Magnetic properties of Co-doped Nb clusters

A. Diaz-Bachs,[1] L. Peters,[1] R. Logemann,[1] V. Chernyy,[1] J. M. Bakker,[2] M. I. Katsnelson,[1] and A. Kirilyuk[1,2,*]

[1]*Radboud University, Institute for Molecules and Materials, Heyendaalseweg 135, 6525 AJ Nijmegen, Netherlands*

[2]*Radboud University, Institute for Molecules and Materials, FELIX Laboratory, Toernooiveld 7c, 6525 ED Nijmegen, Netherlands*

Magnetic deflection experiments on isolated Co-doped Nb clusters demonstrate a strong size dependence of magnetic properties, with large magnetic moments in certain cluster sizes and fully nonmagnetic behavior of others. There are in principle two explanations for this behavior. Either the local moment at the Co site is absent or it is screened by the delocalized electrons of the cluster, i.e., the Kondo effect. In order to reveal the physical origin, first, we established the ground state geometry of the clusters by experimentally obtaining their vibrational spectra and comparing them with a density functional theory study. Then, we performed an analysis based on the Anderson impurity model. It appears that the nonmagnetic clusters are due to the absence of the local Co moment and not due to the Kondo effect. In addition, the magnetic behavior of the clusters can be understood from an inspection of their electronic structure. Here magnetism is favored when the effective hybridization around the chemical potential is small, while the absence of magnetism is signaled by a large effective hybridization around the chemical potential.

I. INTRODUCTION

Electronic correlations constitute the basis of condensed matter physics and are responsible for the enormous wealth of phenomena found in solids, such as (high-T_c) superconductivity [1], charge and spin ordering [2] and fluctuations [3], colossal magnetoresistance [4], metal-insulator transitions [5], half-metallicity [6], the quantum Hall effect [7], and heavy-fermion behavior [8]. Reducing the size, however, leads to an extreme sensitivity of these properties to the atomic arrangement, shape, and effects of the environment. The understanding and control of these size-driven processes is therefore crucial to maintain the pace of developments in nanoscience.

In this miniaturization trend, the ultimate limit is represented by atomic clusters. Such clusters are particles composed of a countable number of atoms, from the diatomic limit up to some thousands or tens of thousands of atoms [9]. Quantum confinement effects entirely govern the behavior of matter in this size regime. The discretized electronic levels lead to sudden changes of the cluster properties, for example when changing the cluster size on an atom-by-atom basis. In the semiconductor technology there is a long-standing interest in systems with discrete energy spectra, such as quantum wells [10] and quantum dots [11].

Obviously the consideration of doped or alloyed instead of pure clusters offers an even broader playground for technological applications. However, doped clusters are also very interesting from a fundamental point of view. For example, it is well known that already for a single magnetic impurity in a nonmagnetic metallic host interesting phenomena such as Friedel oscillations [12] and the Kondo effect [13] can

occur. How would such effects be present in clusters, or would they be present at all? Furthermore, the case of a single magnetic impurity embedded in a discrete host such as a cluster offers a sensitive probe of studying the dependence of the local magnetic moment on the details of the discrete energy spectrum. This could lead to valuable insight in processes reducing the local magnetic moment and/or Kondo screening mechanisms. More precisely, the formation of the atomic magnetic moment is trivially described by the Hund's rules in the case of an isolated atom, but this process is far from trivial in the case of an atom embedded in an interacting host.

Recently, the magnetic moment of a single magnetic impurity in a discrete host was investigated in the framework of the Anderson impurity model [14]. One of the things found was that the local moment grows with increasing host band gap (HOMO-LUMO gap).

Using this relation, the experimentally observed magnetic moments of Cr-doped Au clusters were successfully explained [15]. This demonstrates in particular that the size of the measured local moment follows the trend of the calculated band gap of the host.

In this work we present a comprehensive study of the mechanisms governing the formation of magnetic moments in Co-doped Nb clusters. From magnetic deflection experiments we make the interesting observation that some clusters are strongly magnetic, while others are completely nonmagnetic, in contrast with the Cr-Au case where all measured clusters were found to be magnetic. There are two possibilities for the absence of magnetism in the Nb_xCo clusters. Either there is no local Co magnetic moment or it is screened by the delocalized electrons of the cluster, i.e., the Kondo effect. From the theoretical perspective, the difficulty in explaining the observed magnetic behavior is in the treatment of the electronic correlations. Since it is not clear from the beginning whether correlations effects are weak, intermediate, or

*a.kirilyuk@science.ru.nl

134427-1

strong, it is difficult to decide which theoretical approach is suitable. One could expect correlations to be stronger in small clusters than in their bulk counterparts due to a stronger localization of the wave functions. On the other hand, for the clusters fewer screening channels are present, which could lead to an almost constant Coulomb interaction throughout the cluster [16]. This would render correlation effects unimportant.

Thus, the importance of correlation effects is not known for Nb_xCo clusters *a priori*. To study this, first, we make a comparison of experimental vibrational spectra with those obtained from a density functional theory (DFT) study. This serves two purposes. It provides the ground state geometry of the clusters. Moreover, due to the dependence of the vibrational spectrum on the magnetic moment, the performance of DFT in predicting the magnetic moments can be investigated. Then, in order to obtain a physical understanding of the experimentally observed magnetic behavior, we perform an analysis based on the Anderson impurity model. From this analysis it is observed that the absence of a magnetic moment in the doped clusters is due to an absence of the Co moment and not the Kondo effect. In addition, the magnetic behavior of the Nb_xCo clusters can be understood from an inspection of their electronic structure. Magnetism is favored when the effective hybridization around the chemical potential is small, while the absence of magnetism is signaled by a large effective hybridization around the chemical potential.

Both Co-doped and pure Nb clusters have already been the topic of interest in earlier works. One of the most relevant experimental works on pure Nb clusters is the electric deflection experiment, which showed that cold clusters may attain an anomalous component with very large electric dipole moments [17]. Further, magnetic deflection experiments on pure Nb clusters showed that at very low temperatures the clusters with an odd number of atoms deflect due to a single unpaired spin that is uncoupled from the cluster lattice [18,19]. Far-infrared absorption spectra of small neutral and cationic Nb clusters combined with DFT calculations have revealed their geometries [20]. Compared to pure Nb clusters, not much is known of Co-doped clusters. Experimentally an anion photoelectron spectroscopy study is performed, which showed that the addition of the Co atom for small Nb clusters induces bulklike behavior, i.e., closing of the band gap [21]. From the theoretical side a computational study based on DFT addressed the geometric and magnetic properties finding that Nb_7Co has no net magnetic moment, which means that the magnetic moment of 6 μ_B coming from the Co atom is completely destroyed by interactions with the Nb_x host [22]. The experimental confirmation of this is however completely lacking, which is another reason for conducting a combined experimental and theoretical study.

The rest of this paper is organized as follows. In Sec. II we first present our magnetic deflection experiments. Then, in Sec. III the experimental vibrational spectra are compared with those obtained from density functional theory calculations. Based on the ground state geometries obtained from this comparison, we perform a discussion based on the Anderson impurity model in Sec. IV to address the presence or absence of magnetic moments in Nb_xCo clusters. Finally, in Sec. V we present our conclusions.

II. MAGNETIC DEFLECTION EXPERIMENTS

A. Stern-Gerlach type of setup

The magnetic moments of the Nb_xCo clusters were obtained by means of a Stern-Gerlach-like setup [23]. This setup consists mainly of three parts: the source, the magnet, and the position-sensitive time-of-flight mass spectrometer (PSTOFMS). The source is of Milani–de Heer type [24]. The clusters are produced in the source chamber by ablation of a Nb_xCo_y ($x = 95\%$, $y = 5\%$) rod due to a Nd:YAG laser producing 532 nm light. More precisely, this laser is focused on the rod, which is inside a cavity of a tuneable volume. The cavity is connected to a pulsed valve, responsible for introducing pulses of helium, which is the carrier gas; i.e., it is responsible for the transport of the clusters across the setup. The cavity is also coupled to a nozzle. Due to a pressure gradient across the nozzle, the clusters expand supersonically. The actual creation and cooling of the clusters takes place inside the cavity. In our setup the source can be cooled down to 20 K due to a cold head. Once the cluster beam has left the cavity, it crosses a conical skimmer of 1 mm width. After the clusters are skimmed they reach a chopper, which has two purposes: cluster selection and measurement of their velocity. Then, after the chopper there are two slits to narrow the beam in both the horizontal and vertical direction. After the slits, the cluster beam reaches the magnet, i.e., a two-wire Rabi design electromagnet [25]. The magnet produces an inhomogeneous magnetic field that can reach a maximum strength of 2.4 T and gradient of 650 T/m. The spins of the cluster are aligned by the magnetic field, while the cluster is deflected due to the gradient in the field. For the calibration of the magnet, aluminium atoms were chosen, since they are easy to produce and their magnetic properties are well known ($\mu = 1/3 \, \mu_B$, $J = 1/2$, $m_J = \pm 1/2$).

After the magnet the clusters have to travel 1 m before they reach the PSTOFMS. In order to detect the clusters, they are ionized by an excimer laser producing an ultraviolet beam of 193 nm. The ionized clusters can then be directed by the electric fields of the PSTOFMS plates towards the micro channel plate (MCP) where they are detected. After the detection of the cluster, its time-of-flight is known. This time-of-flight linearly depends on the deflection of the cluster, where the proportionality constant is obtained from another calibration. For this calibration, a narrow slit is placed in the path of the excimer beam. Then, by moving the slit, the time-of-flight can be determined for each corresponding slit position, i.e., the position where the clusters will be ionized, describing the correlation between time-of-flight and deflection. Since the determined proportionality constant is known to scale as the square root of the mass, it is only necessary to perform the calibration for one specific cluster size.

From the measurement of the deflection x via the time-of-flight, the mass m of the cluster, and its velocity v by means of the chopper, the average magnetic moment is determined from

$$\langle \mu \rangle = \frac{xmv^2}{KB}. \tag{1}$$

Here B is the magnetic field strength and K is a constant that depends on the setup. This constant includes the gradient of
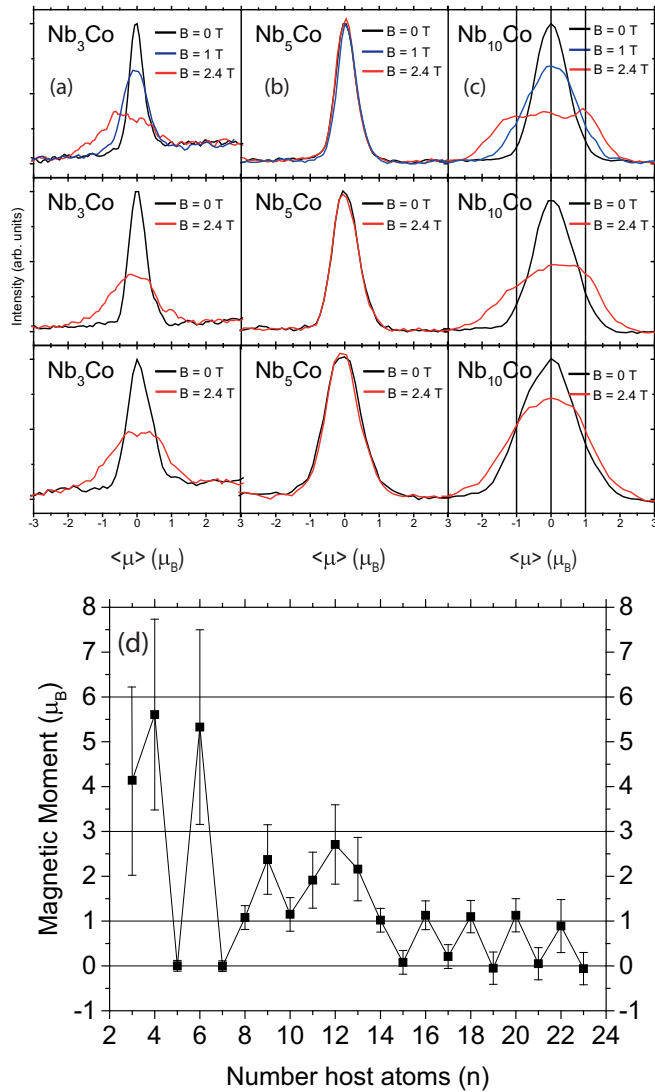
FIG. 1. The top three columns contain the different deflection profiles observed for the Co-doped Nb clusters. (a) Single-sided deflection profile for Nb$_3$Co, which indicates a superparamagnetic cluster. (b) Profile of Nb$_5$Co showing no deflection, which corresponds to a nonmagnetic cluster. (c) Two-sided deflection profile for Nb$_{10}$Co, which refers to an atomic-like cluster. The black, blue, and red lines correspond to the situations without a magnetic field and with a 1 T and a 2.4 T magnetic field. Further, the first row corresponds to deflections measured at 25 K, the second row at 40 K, and the third row at 70 K. For the x axis of all deflection profiles, the deflection is converted to the averaged magnetic moment via Eq. (1). In the bottom figure indicated with (d), the magnetic moment as a function of cluster size is presented with n corresponding to the number of host (Nb) atoms. Here the error bars are computed from the uncertainty in the velocity of the cluster and the magnetic field.

the magnet, which is determined from the calibration by the aluminium atoms.

During the measurements we observed three different deflection [or equivalently average magnetic moment via Eq. (1)] profiles; see Figs. 1(a)–1(c). The method we used to obtain the actual value of the deflection depends on the observed deflection profile. In the case of a deflection profile centered at

zero [Fig. 1(b)] we used a Gaussian fit, where the position of the peak of the Gaussian corresponds to the "deflection." For the double-sided deflection profile [Fig. 1(c)] three peaks can be observed. Here the peak at 0 is due to the spin relaxation by the coupling to the lattice, which can be in principle reduced by increasing the carrier gas pressure [19]. Therefore, the deflection should be determined from the peaks away from zero. For this purpose we used three Gaussians to fit the profile, where the deflection is determined from the peak position of the Gaussians not located at zero. Finally, for single-sided deflection [Fig. 1(a)] the profile is in general asymmetric, which makes a fit by a Gaussian inappropriate. In this case we take the position of the average of the peak as the deflection.

In Eq. (1), the quantity $\langle \mu \rangle$ corresponds to the measured average magnetic moment of the clusters. However, not for all the three observed deflection profiles, this corresponds to the actual magnetic moment of the cluster. While it does for no deflection and double-sided deflection, it does not for single-sided deflection. Obviously, no deflection corresponds to a nonmagnetic cluster. Double-sided deflection corresponds to atomic-like clusters, i.e., clusters where the magnetic moment can freely rotate. In contrast, single-sided deflection corresponds to superparamagnetic clusters with the magnetic moment coupled to the lattice. More precisely, due to the anisotropy present in the cluster the magnetic moment is not free to rotate, but points along the easy axis. Then, due to the presence of a finite temperature, not all clusters have their magnetic moment aligned with the magnetic field. Therefore, the measured average magnetic moment needs to be related to the actual magnetic moment of the cluster [26–28]. For isolated clusters this is typically done by the Langevin-Debye function. In the limit of a small magnetic field this leads to the following relation:

$$M = \frac{1}{3} \frac{\langle \mu \rangle^2 B}{k_B T},$$ (2)

where M is the magnetic moment of the cluster, T the temperature, and k_B the Boltzmann constant. The temperature of the cluster is difficult to obtain due to differences in its rotational, vibrational, and translational temperatures. In this work the nozzle temperature is taken. On the other hand the translational temperature determined from the cluster's speed is roughly 15–20 K higher. This uncertainty is incorporated in the error bars.

B. Results: Magnetic moments

The results of the Stern-Gerlach experiments performed on the Co-doped Nb clusters at temperatures of 25 K (first row), 40 K (second row), and 70 K (third row) are presented in Fig. 1. Here Figs. 1(a), 1(b) and 1(c) correspond to the three typical deflection profiles that were observed. The black, blue, and red lines in the deflection profiles correspond respectively to the situation without a magnetic field and with a 1 T and 2.4 T magnetic field. In Fig. 1(d) the measured magnetic moments in μ_B are presented as a function of cluster size with n corresponding to the number of host (Nb) atoms. These magnetic moments are obtained by taking an average of the magnetic moments observed for the different considered temperatures and external magnetic fields.

Figure 1(a) for Nb$_3$Co shows a typical single-sided deflection profile indicating superparamagnetic behavior, which upon an increase of temperature becomes an asymmetric double-sided deflection. Other clusters showing a single-sided deflection profile were Nb$_4$Co, Nb$_6$Co, Nb$_9$Co, Nb$_{11}$Co, Nb$_{12}$Co, and Nb$_{13}$Co. Then, Fig. 1(b) for Nb$_5$Co presents the situation with no deflection, which corresponds to a nonmagnetic cluster. The other clusters showing no deflection were Nb$_7$Co and all the even numbered clusters (i.e., with n odd) studied with $n > 15$. The last observed deflection profile is depicted in Fig. 1(c), where for Nb$_{10}$Co an example of a two-sided deflection is given, which refers to an atomic-like cluster. This profile is characterized by 3 peaks, 2 peaks at $\pm 1 \, \mu_B$, and an additional peak at 0 μ_B. Two-sided deflection was also observed for all clusters containing an odd number of atoms (i.e., with n even) and with $n \geqslant 14$.

From the magnetic moments as a function of cluster size presented in Fig. 1(d) it seems that the clusters can be divided into two regions. For clusters with $n \geqslant 14$ the magnetic to nonmagnetic behavior appears to be exactly determined by having an odd or even number of atoms in the cluster. An odd number of atoms in the cluster corresponds to the situation of at least one unpaired electron and thus at least a moment of 1 μ_B. For an even number of atoms, all the electrons can be paired. Note that the magnetic behavior of pure Nb clusters was indeed explained in this way [18]. Then, there is the regime of clusters with $n < 14$, where the magnetic behavior clearly cannot be explained due the presence or absence of a single unpaired electron. In this region strong fluctuations in the magnetic moment can be observed by just adding or removing a single Nb atom. For example, Nb$_4$Co is strongly magnetic, while Nb$_5$Co is completely nonmagnetic. Then, again adding just one Nb atom leads to Nb$_6$Co which is again strongly magnetic. On the other hand Nb$_7$Co is again nonmagnetic.

It can also be observed that there is no cluster with a magnetic moment larger than that of an isolated Co atom. An isolated Co atom has 7 3d electrons leading to a total moment of 6 μ_B, where both the spin and orbital moment contribute 3 μ_B. This indicates that either the Co atom is not very effective in inducing magnetic moments in the Nb$_x$ host or a large part of the Co moment is absent due to interactions with the Nb$_x$ host. Based on an inspection of previous works the latter explanation seems to be the most plausible. For example, in Ref. [22] it is shown by means of a DFT study on Nb$_x$Co clusters that roughly 20%–50% of the total magnetic moment can come from the Nb host. It should be mentioned that in this study only the spin magnetic moment is considered. However, from for example Refs. [29] and [30] it is well established for pure Co clusters that the orbital contribution can be substantial, about 0.7 μ_B per Co atom. A similar observation is made for Co clusters deposited on Pt(111) [31]. Although being substantial, it is still largely quenched with respect to the 3 μ_B of the isolated atom. Besides the orbital moment of the Co atom, also its spin moment is known to be reduced in Nb$_x$Co [22] and pure Co clusters [29,30,32,33]. For the Nb$_x$Co clusters it is found to be about 1–2 μ_B. Based on these observations we expect that the spin moment of the Nb$_x$Co clusters can be attributed to both the Nb$_x$ host and Co atom. On the other hand the orbital moment is expected to come from the Co atom and to be quenched to roughly 0.7 μ_B.

III. VIBRATIONAL SPECTRA: GEOMETRIC AND MAGNETIC STRUCTURE

In this section we perform a comparison of experimental vibrational spectra with those obtained from a DFT study. This serves two purposes. First, due to the dependence of the vibrational spectrum on the magnetic moment, the performance of DFT in predicting the magnetic moments can be investigated. Second, it provides the ground state geometry of the clusters. These ground state geometries are required as an input in Sec. IV to obtain a physical understanding of the observed magnetic behavior in Sec. II.

A. Experimental details

In order to record the vibrational spectra we coupled our cluster setup to the Free Electron Laser for Intra-Cavity Experiments (FELICE) [34]. Below a brief description of the experimental setup is given and for more details the reader is referred to Refs. [35,36]. The clusters are produced in an ablation-type cluster source in a growth channel filled by a helium carrier gas prior to ablation of a Nb$_x$Co$_y$ ($x = 95\%$, $y = 5\%$) rod by a Nd:YAG laser (532 nm). The temperature of the extension tube, which is attached to the cluster source for better cluster thermalization, is 77 K. After expansion in the source chamber, the mixture of clusters and carrier gas is skimmed. This results in the formation of a molecular beam that is shaped by a slit with a width of 0.45 mm. The interaction between the IR light and the molecular beam takes place in the center of the extraction region of the RETOF mass spectrometer with a 35° angle between the two beams. The IR pulse energies inside the FELICE cavity range between 0.2 and 0.6 J over the IR scans. The IR pulse consists of a 9 μs long train of micropulses with 1 ns time delay between them. The clusters are ionized by a frequency-doubled dye laser with a photon energy of 5.4 eV entering the extraction region at a ~90° angle with respect to the cluster beam. The frequency of the ionizing laser is chosen just below the ionization potential, and in the absence of the IR laser, only a small ion yield is observed for each mass. When the IR laser is resonant, the number of neutrals that can be ionized is increased, leading to a frequency-dependent gain upon ionization; all species formed are accelerated into the RETOF flight tube by extraction plates with static voltages. The experiment operates at twice the FELICE frequency which allows us to record a signal with [$I_{\text{IR+UV}}(\omega)$] and without (I_{UV}) IR radiation in a shot-to-shot manner. The experimental IR curves are presented in terms of gain spectra [$G(\omega)$] calculated as

$$G(\omega) = \frac{I_{\text{IR+UV}}(\omega) - I_{\text{UV}}}{I_{\text{UV}}}, \qquad (3)$$

at an IR frequency ω, and are for the IR pulse energy corrected.

B. Computational details

For the calculation of the vibrational spectra we employed the DFT implementation of the Vienna *ab initio* simulation package (VASP) [37]. The projector augmented wave (PAW) method [38,39] in combination with the Perdew, Burke, and Ernzerhof (PBE) functional is used [40]. For all cluster sizes we searched for the lowest-energy geometries by using a genetic
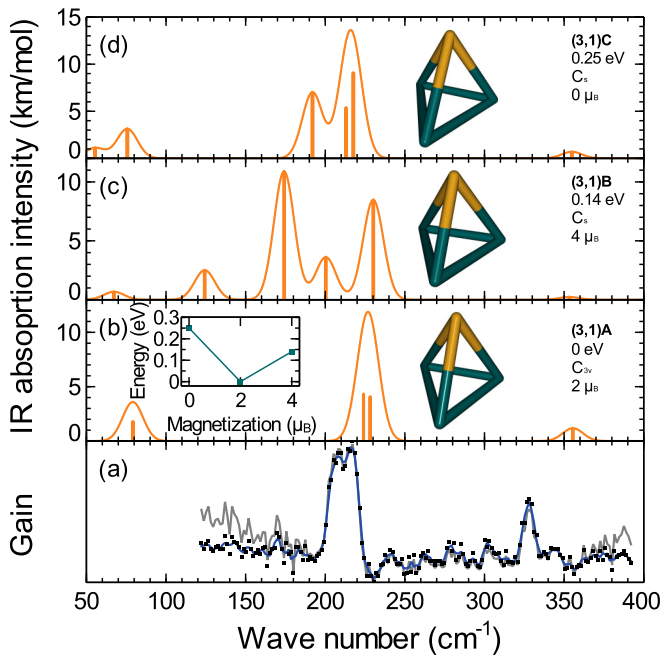
FIG. 2. Experimental [panel (a), squares] and calculated [(b)–(d)] IR spectra of Nb$_3$Co. The blue line is a three-point adjacent average of the experimental data. The gray dashed line indicates the IR power corrected spectrum. The calculated discrete vibrational frequencies (orange vertical lines) are convoluted with a 15 cm^{-1} FWHM Gaussian line shape function (orange). For the geometries green and gold are used for Nb and Co, respectively. The inset graph shows the energy as a function of the magnetization for the different magnetic states.

algorithm (GA) [41] in combination with DFT. The details of the used method can be found in Ref. [42]. In addition, we also considered conformations previously reported in the literature (Nb$_3$Co, Nb$_4$Co, Nb$_5$Co, Nb$_6$Co, Nb$_7$Co) [22] and reoptimized the mentioned structures. For some clusters the GA results were equal to those already found in the literature, while for other clusters additional geometries lower in energy were obtained (see Secs. III C 1–III C 6 for details). Further, for the PAWs an energy cutoff of 4293 eV is used. All forces were minimized below 10^{-3} eV/Å. In order to eliminate intercluster interactions, the clusters were placed in a cubic periodic box with 16 Å dimensions. For the calculations, a single k point (Γ) is used.

C. Results: Geometric and magnetic structure

In the following, we will present experimental and calculated spectra for the two or three lowest energy isomers. The calculated geometries of the clusters are presented by a stick model; i.e., the clusters are presented by connected sticks. Here green corresponds to Nb and gold to Co. Further, to facilitate the comparison of the experimental and calculated results, the experimental spectra are shown with black squares accompanied by a three-point adjacent average (blue line). The gray dashed line indicates the IR power corrected experimental spectrum. The calculated harmonic vibrational frequencies (vertical sticks) are convoluted with a 15 cm^{-1} FWHM Gaussian line shape function. All frequencies for the
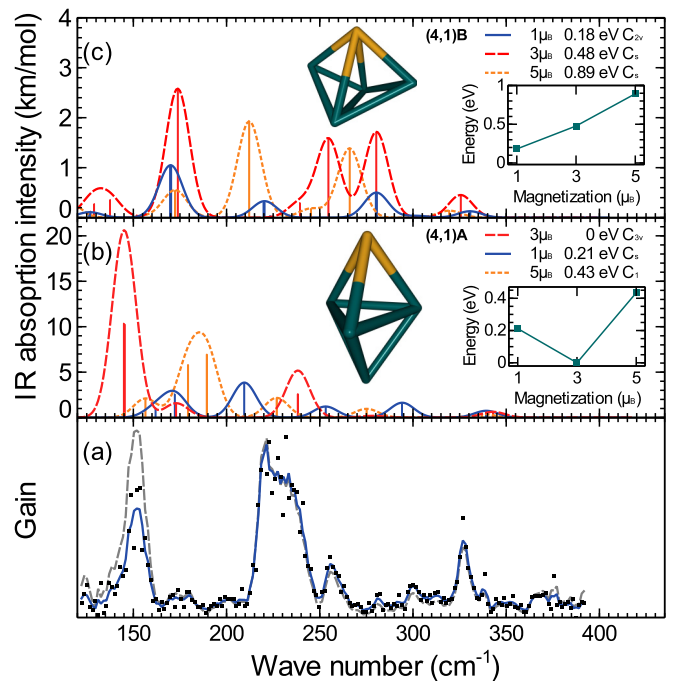

FIG. 3. Experimental [panel (a)] and calculated [(b)–(c)] vibrational spectra of Nb$_4$Co. The insets show the energy as a function of magnetization for each geometry.

structures presented in this work are unscaled and the energies contain the zero-point vibrational energies (ZPVE). Finally, the insets of the figures below show the energy as a function of magnetization for the presented geometries with respect to that of the ground state.

1. Nb$_3$Co

For Nb$_3$Co a trigonal pyramid is found with three different magnetic states. Here the Nb-Nb and Nb-Co distances differ slightly between the magnetic configurations.

In Figs. 2(b)–2(d) the corresponding geometries are shown. The magnetic $M = 2\,\mu_B$ (3,1)A geometry is lowest in energy, with (3,1)B and (3,1)C 0.14 eV and 0.25 eV higher, respectively. Note that geometry (3,1)A has been reported previously also as the ground state in Ref. [22]. The symmetry point group depends on the magnetization, with C_{3v} for (3,1)A and C_s for (3,1)B and (3,1)C. This difference in symmetry results in significant differences in the vibrational spectra.

Figure 2 shows that the vibrational spectrum of (3,1)A with modes at 224, 228, and 356 cm^{-1} provides the best match to the experimental modes at 212 and 328 cm^{-1} and also explains the doublet structure of the band at 212 cm^{-1}. The vibrational spectra of (3,1)B and (3,1)C contain vibrational modes in the range 125–220 cm^{-1} where no clear experimental modes are observed. Therefore, geometry (3,1)A in the $M = 2\,\mu_B$ state is assigned as the ground state of Nb$_3$Co.

2. Nb$_4$Co

In the experimental spectrum of Nb$_4$Co presented in Fig. 3(a), at least four modes can be distinguished, at 150, 230, 255, and 325 cm^{-1}. The two geometries lowest in energy are
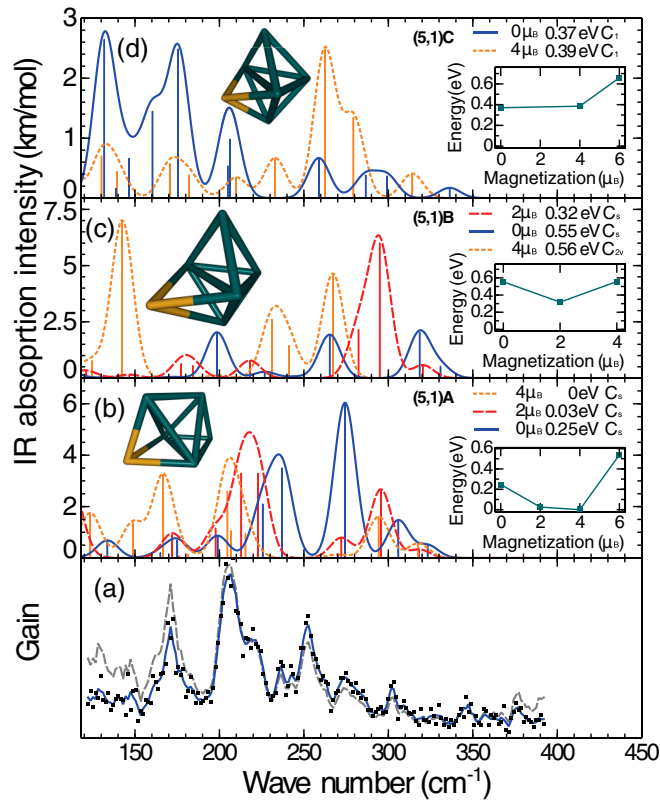
FIG. 4. Experimental [panel (a)] and calculated [(b)–(d)] vibrational spectra of Nb$_5$Co.

shown in Figs. 3(b) and 3(c). Geometry (4,1)A with $M = 3\,\mu_B$ is the lowest in energy and has C_{3v} point group symmetry. Geometry (4,1)A consists of a trigonal bipyramid, where Nb and Co are the axial atoms. In contrast, in geometry (4,1)B the Co atom is part of the equatorial triangle. For geometry (4,1)B the $M = 1\,\mu_B$ state is the lowest in energy and is 0.18 eV higher compared to the lowest of (4,1)A. Note that both (4,1)A and (4,1)B are previously reported in Ref. [22], where (4,1)A with $M = 3\,\mu_B$ was also found to be the lowest in energy. The vibrational spectrum of (4,1)A with $M = 3\,\mu_B$ consists of two large modes at 145 and 238 cm^{-1} and smaller modes at 173, 278, and 342 cm^{-1}, and matches the experimental spectrum. The vibrational spectrum of (4,1)A with $M = 3\,\mu_B$ is the only spectrum with two major modes around 150 and 230 cm^{-1}. Therefore, we tentatively assign geometry (4,1)A with $M = 3\,\mu_B$ to be the ground state of Nb$_4$Co.

3. Nb$_5$Co

In Figs. 4(b)–4(d) the three geometries found to be lowest in energy for Nb$_5$Co are presented. Geometry (5,1)A consists of a dimer-capped rhombus with C_s point group symmetry for all considered magnetic states and has been previously reported in Ref. [22] to be the lowest in energy for the $M = 4\,\mu_B$ state. We also find geometry (5,1)A in the $M = 4\,\mu_B$ state to be the lowest in energy, although the $M = 2\,\mu_B$ state is only 0.03 eV higher. Geometries (5,1)B and (5,1)C both consist of a distorted Nb$_5$ bipyramid with one of the faces of the bipyramid capped by the Co atom. Geometries (5,1)B and (5,1)C differ in the distance of the Co atom to the bipyramid.

Whereas for the (5,1)B geometry the $M = 2\,\mu_B$ state is the lowest in energy, the (5,1)C geometry has a nonmagnetic ground state which is 0.37 eV higher in energy compared to (5,1)A. The experimental spectrum of Nb$_5$Co in Fig. 4(a) shows three major bands at 170, 205, and 250 cm^{-1}, where the internal structure of the band at 205 cm^{-1} indicates at least a second mode at 220 cm^{-1}. A smaller vibrational mode is present at 275 cm^{-1}. If the calculated spectra of Fig. 4(b)–4(d) are compared to that of Fig. 4(a), both (5,1)A $M = 4\,\mu_B$ and (5,1)C $M = 0\,\mu_B$ can only partially explain the experimental spectrum. Whereas (5,1)C $M = 4\,\mu_B$ resembles the experimental spectrum below 230 cm^{-1}, the structure around 250 cm^{-1} is not present in the calculated spectrum. Due to the similar vibrational spectrum and the low difference in energy between (5,1)A $M = 2\,\mu_B$ and $M = 4\,\mu_B$, the former cannot be excluded based on IR vibrational spectroscopy. The vibrational spectrum of (5,1)C $M = 0\,\mu_B$ agrees for the modes above 250 cm^{-1}, but deviates significantly in the relative IR absorption intensities between modes compared to the experimentally observed gain. Therefore, the IR gain spectrum of Nb$_5$Co might be due to the geometry (5,1)A with $M = 2\,\mu_B$ or $M = 4\,\mu_B$, or geometry (5,1)C $M = 0\,\mu_B$. However, due to the finite temperature at which the experiment is performed, the vibrational spectrum might also be due to a combination of different geometries and magnetic states. On the other hand, the magnetic deflection experiments (see Sec. II) were performed at a lower temperature than the vibrational experiments and strictly found Nb$_5$Co to be nonmagnetic. Therefore, the (5,1)C geometry corresponding to the $M = 0\,\mu_B$ state is ascribed to be the ground state.

4. Nb$_6$Co

The two geometries that were found to be the lowest in energy for Nb$_6$Co are shown in Figs. 5(b) and 5(c). Here geometry (6,1)A consists of a distorted pentagon with both sides capped with a single Nb atom. Geometry (6,1)A in the $M = 3\,\mu_B$ state is obtained as the lowest in energy. All magnetic states of the (6,1)A geometry have a C_1 point group symmetry. Geometry (6,1)B consists of two stacked Nb$_3$ triangles, where the top triangle is capped with a Co atom. For this geometry the $M = 1\,\mu_B$ state is the lowest in energy and has a C_{3v} point group symmetry. The experimental IR spectrum of Nb$_6$Co is shown in Fig. 5(a) and contains a dominant mode at 270 cm^{-1} and two smaller modes at 200 and 220 cm^{-1}. The vibrational spectrum of (6,1)B $M = 1\,\mu_B$ provides the best match to the experimental spectrum with a single dominant mode at 256 cm^{-1} and several smaller modes constituting two bands at 190 and 210 cm^{-1}. In the vibrational spectrum of (6,1)A the bands at 220 and 264 cm^{-1} have similar IR absorption intensities, which is in disagreement with the experimentally observed relative difference between these bands. All other geometries have significant vibrational modes below 190 cm^{-1} where experimentally no modes are observed. Therefore, the (6,1)B geometry with the $M = 1\,\mu_B$ state is assigned to the ground state of Nb$_6$Co.

5. Nb$_7$Co

The experimental spectrum of Nb$_7$Co in Fig. 6(a) has arguably the poorest signal-to-noise ratio of all spectra shown
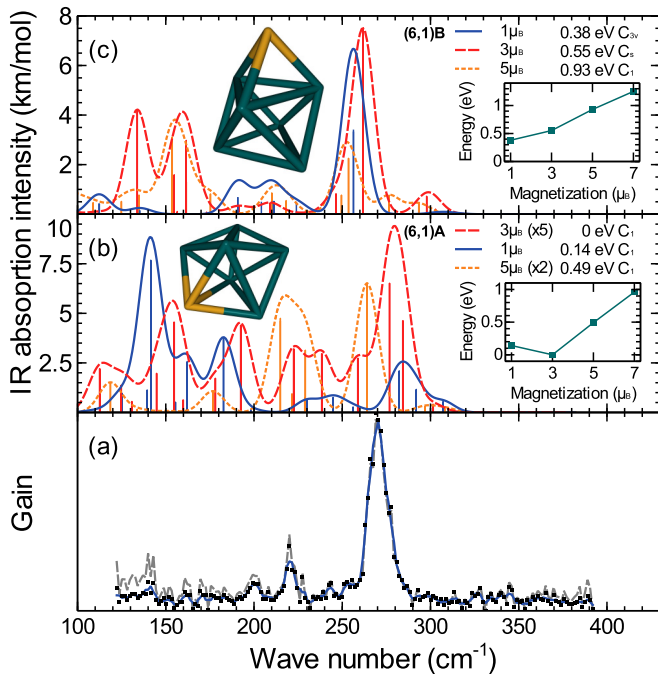
FIG. 5. Experimental [panel (a)] and calculated [(b)–(c)] vibrational spectra of Nb$_6$Co. The IR absorption intensity of (6,1)A $M = 3\,\mu_B$ and $M = 5\,\mu_B$ are enhanced by a factor of 5 and 2, respectively, to increase visibility.

FIG. 6. Experimental [panel (a)] and calculated [(b)–(d)] vibrational spectra of Nb$_7$Co.

here. The spectrum shows one clear band centered around 260 cm^{-1}, and some less pronounced structure at lower frequencies. The three geometries lowest in energy are shown in Figs. 6(b)–6(d). All geometries found have either one symmetry plane or no symmetry at all. Geometry (7,1)A consists of a distorted pentagonal Nb bipyramid, with one of the faces capped by a Co atom.

The lowest energy spin state of geometry (7,1)A has a magnetic moment of $M = 0\,\mu_B$, although the triplet structure is only 0.06 eV higher in energy. Structure (7,1)A was also previously reported as the lowest in energy [22]. A second structure (7,1)B is formed by a Nb$_4$Co square pyramid with a Co apex; three more Nb atoms form a triangle parallel to the pyramid base. Structure (7,1)C is essentially the same structure as (7,1)B now with a full Nb pyramid, and the Co part of the triangle. In contrast to structure (7,1)A, the magnetic ground states of geometries (7,1)B and (7,1)C are magnetic, both with $M = 2\,\mu_B$. Due to the low symmetry of all structures, their vibrational spectra contain many vibrational modes. Structure (7,1)C's spectra all extend to higher frequency than those for either (7,1)A and (7,1)B.

The single experimental band at 260 cm^{-1} can be explained by both (7,1)A $M = 0\,\mu_B$ and (7,1)B. Both spectra do not match the observed structure in the lower frequency region particularly well. That being so, we cannot assign the spectrum to one particular structure or magnetic state. As will be discussed later, this lack of definite assignment will not change the conclusions regarding the nature of the magnetic structure observed in the Stern-Gerlach deflection experiments.
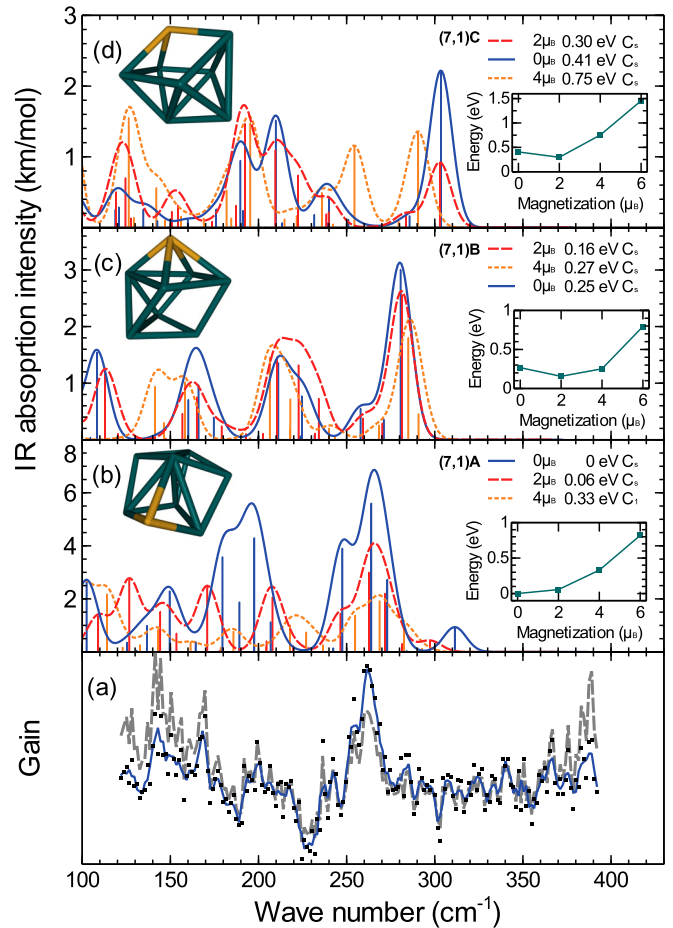
6. Nb$_9$Co

Figure 7(a) shows the IR gain spectrum of Nb$_9$Co. Although this figure is not very well resolved, at least bands at 205, 240, and 280 cm^{-1} can be identified. In Figs. 7(b)–7(d) the three Nb$_9$Co geometries that were found to be the lowest in energy are presented. Here geometry (9,1)A consists of a Nb$_4$ rhombus stacked with a Nb$_5$ pentagon capped by a Co atom. Note that geometry (9,1)A is distorted such that only a mirror plane symmetry remains. The geometry indicated by (9,1)B consists of two stacked Nb$_4$ squares, where the two open faces are capped by a Nb and Co atom. The (9,1)C geometry is best described (yet poorly) by a distorted hexagon with a Nb in the center and a Co atom occupying a corner, and capped by a Nb$_3$ triangle. Here for the geometry (9,1)C in the states $M = 2$ and $M = 0\,\mu_B$ there is no symmetry, while in the $M = 4\,\mu_B$ state there is only a mirror plane. For geometry (9,1)C the $M = 2\,\mu_B$ state is found to be the lowest in energy, while the $M = 0\,\mu_B$ state is 0.12 eV higher in energy. If the calculated vibrational spectra of Figs. 7(b)–7(d) are compared to the experimental spectrum, geometry (9,1)C with $M = 2$ and $M = 0$ provides the best match with dominant bands around 205 and 285 cm^{-1} and an intermediate mode in between. Therefore, the ground state of the Nb$_9$Co cluster is described by the (9,1)C geometry.
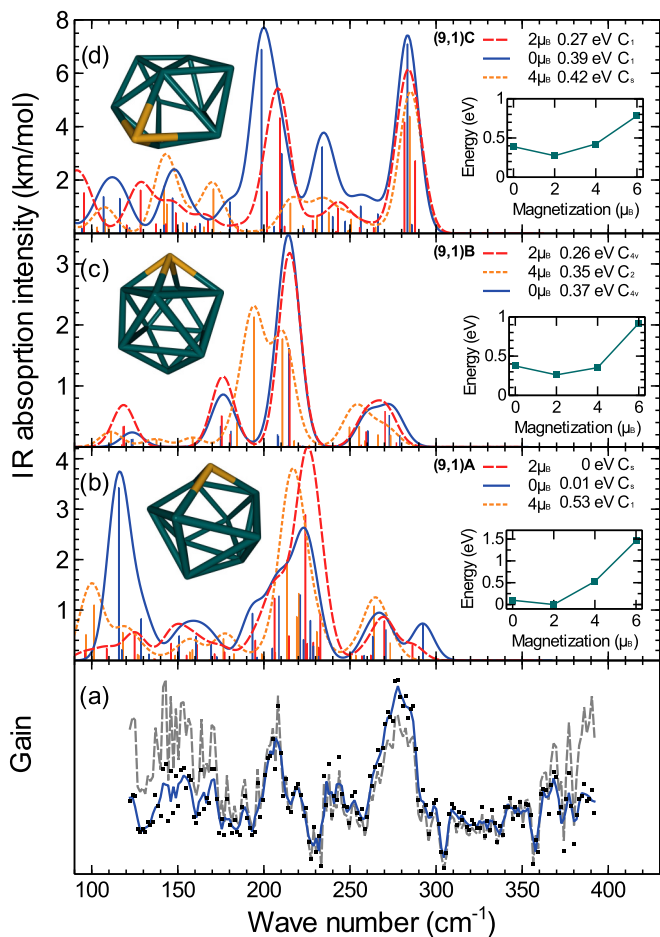
FIG. 7. Experimental [panel (a)] and calculated [(b)–(d)] vibrational spectra of Nb$_9$Co.

D. Comparison with magnetic deflection results

It is interesting to compare the magnetic moments obtained from the magnetic deflection experiments described in Sec. II with those obtained above from an inspection of the vibrational spectra. In Table I the second column contains the total magnetic moments of the Nb$_x$Co clusters obtained from the best match of the calculated DFT vibrational spectra compared to experiment. For some clusters multiple magnetic moments are given, because for them it was not clear which vibrational

TABLE I. Here the second column corresponds to the total magnetic moments of the Nb$_x$Co clusters obtained from the best match of the calculated DFT vibrational spectra with respect to experiment. The third column contains the magnetic moments obtained from the magnetic deflection experiments presented in Sec. II.

Cluster	M_{vib} (μ_B)	M_{exp} (μ_B)
Nb$_3$Co	2	4.1
Nb$_4$Co	3	5.6
Nb$_5$Co	0, 2, 4	0.0
Nb$_6$Co	1	5.3
Nb$_7$Co	0	0.0
Nb$_9$Co	0, 2	2.4

spectrum matches the best with experiment. The third column corresponds to the magnetic moments observed in the magnetic deflection experiments [see Fig. 1(d)].

Except for Nb$_5$Co it appears that the magnetic moments predicted by the magnetic deflection experiments are substantially larger. Part of this difference is due to not taking into account the orbital contribution to the magnetic moment within the DFT calculations. However, even if we would have considered them, it is well known that orbital moments can be highly underestimated in DFT especially for clusters [29]. Based on the orbital moment observed in pure Co clusters and Co clusters deposited on Pt(111) a value of about 0.7 μ_B is roughly expected. This together with the observation made in Ref. [22] that the Nb host contributes about 20%–50% to the total magnetic moment of the Nb$_x$Co clusters means that the spin contribution is underestimated within DFT.

Unfortunately, for Nb$_5$Co and Nb$_9$Co we cannot be conclusive about the magnetic moment obtained from an inspection of the vibrational spectra. For Nb$_5$Co the zero magnetic moment would be in agreement with the magnetic deflection experiment, but this state is 0.37 eV higher in energy than the calculated ground state. Note that for Nb$_6$Co and Nb$_7$Co the best match of the calculated spectrum with experiment was also for a state higher in energy than the ground state, respectively 0.38 and 0.16 eV. On the other hand for Nb$_3$Co and Nb$_4$Co the spectrum calculated for the ground state provided the best match with experiment. For Nb$_9$Co the state with a magnetic moment of 2 μ_B would be the closest to the result of the magnetic deflection experiment. Here the state with a moment of 2 μ_B is 0.27 eV higher in energy than the ground state.

IV. THEORETICAL INVESTIGATION BASED ON THE ANDERSON IMPURITY MODEL

In this section the physical origin is explained of the magnetic behavior obtained from the magnetic deflection experiments presented in Sec. II. For example, it will be understood why some clusters are strongly magnetic, while others are nonmagnetic. For this purpose an analysis based on the Anderson impurity is performed, where the ground state geometries obtained in Sec. III are required as an input.

A. Theoretical background

There are two possible explanations for some Nb$_x$Co clusters being nonmagnetic. It can be nonmagnetic, because interactions of the Co atom with the Nb$_x$ host destroy the local moment at the Co site. More precisely, there is a competition between the Jahn-Teller distortion working against the formation of a magnetic moment and the exchange interaction between Nb and Co preferring the existence of a magnetic moment. Another possibility is that the local moment at the Co site is screened by the delocalized electrons in the cluster, i.e., the Kondo effect. For both mechanisms it is crucial to understand physically when a local moment is formed on the Co site. In the case of a magnetic (transition-metal) impurity resolved in a metallic nonmagnetic host this is well established within the celebrated Anderson impurity model

[13,43,44],

$$H = \sum_{k,\sigma} \epsilon_{k\sigma} c_{k\sigma}^\dagger c_{k\sigma} + \sum_\sigma E_{d\sigma} d_\sigma^\dagger d_\sigma + U n_{d\uparrow} n_{d\downarrow}$$

$$+ \sum_{k,\sigma} V(d_\sigma^\dagger c_{k\sigma} + c_{k\sigma}^\dagger d_\sigma). \qquad (4)$$

Here $E_{d\sigma}$ is the single-particle impurity energy level and U is the on-site Coulomb repulsion between the impurity states. Further, the dispersion of the noninteracting electronic bath is given by $\epsilon_{k\sigma}$. The coupling between the impurity and bath states is described by V. Within this model the formation of a local moment depends on a delicate interplay between the on-site Coulomb interaction, the coupling strength between the impurity and bath states, the position of the bare impurity level (or equivalently the filling), and the positions of the bath energy levels (the dispersion). Within the static mean-field approximation the criterion for a local moment to exist is $U/\Gamma > \pi$. Here $2\Gamma = \pi V^2 \rho(E_F)$ is the effective hybridization, i.e., broadening of the impurity E_d level, where $\rho(E_F)$ is the density of impurity states at the Fermi level. From this criterion it is clear that a large on-site Coulomb interaction and small coupling between the impurity and bath are favorable for a local moment to exist.

It is well known that Kondo physics occurs for the model described by Eq. (5) at half filling and in the limit where the hybridization can be treated perturbatively. More precisely, it can be shown that in this regime the virtual spin-flip scatterings of the bath electrons against the local impurity moment are the dominant processes occurring in the system. At low enough temperatures, below the Kondo temperature, they start to screen the local moment. For half filling and by treating the hybridization perturbatively, the Kondo temperature T_K can be estimated via

$$T_L = U \left(\frac{\Gamma}{2U}\right)^{1/2} \exp\left[\frac{-\pi |E_d||E_d + U|}{2U\Gamma}\right], \qquad (5)$$

where the Kondo temperature is equal to $T_K = 0.041 T_L$ [13]. The Kondo effect for very small systems has been been the subject of study already for several decades, e.g., for quantum dots. Theoretically, the Kondo effect was predicted to take place in quantum dots [45–47]. A few years later experiments confirmed these predictions [48,49].

Although less studied within the Anderson impurity model, the situation of a magnetic impurity resolved in a semiconductor or equivalently a bulk host with a band gap has also been addressed [14,50]. It has been demonstrated that a local magnetic moment on the impurity is stabilized by the introduction of a band gap. In more detail a local moment can be formed even when the criterion above is not satisfied. Furthermore, the magnitude of the local moment increases with increasing band gap.

In Ref. [14] the investigation of the Anderson impurity model for an impurity in a gapped host is extended to the situation of a finite-sized host. Interestingly, it was found that on average the local moment grows with increasing band gap (HOMO-LUMO gap). Here on average should be understood as the local moment averaged over a number of random configurations of the discrete host energy levels for a fixed band gap. Further, it has been shown that in the regimes where

$V \ll E_g$ or $V \gg E_g$, the magnitude of the local moment merely depends on the size of the band gap (E_g) and not on the exact positions of the discrete energy levels of the host. Namely, for $V \ll E_g$ the effect of the hybridization is small no matter what the exact arrangement of the host energy levels is, while for $V \gg E_g$ the impurity level hybridizes with all host levels anyway. However, for the regime in between, $V \sim E_g$, the local moment strongly depends on the exact positions of the host energy levels. In Ref. [15] these findings were successfully used to interpret the experimentally observed magnetic moments of Au_xCr^+ clusters. For example, the trend of the Au_x host band gap was found to exactly follow that of the magnetic moment of the Au_xCr^+ clusters.

B. Computational details

In this work we perform for the Nb_xCo clusters an analysis based on the Anderson impurity model. First, in the same spirit as in Ref. [15] we will demonstrate and explain why this does not work. Second, we show what extra has to be done in order to obtain a successful understanding. For this purpose the density functional theory (DFT) [51,52] is employed within the full-potential linear muffin-tin orbital method [53]. The local density approximation (LDA) exchange-correlation functional is used in the formulation of Perdew and Wang [54]. For the Nb atoms the main valence basis functions were $4d$, $5s$, and $5p$ states, while $4s$ and $4p$ states were treated as pseudocore in a second energy set [53]. In the case of Co, the $3s$ and $3p$ states were treated as pseudocore, and the $3d$, $4s$, and $4p$ states as the main valence states. In all calculations the valence states were treated scalar-relativistically (without spin-orbit coupling). Since the employed DFT code works in k space, a supercell approach was used. A large unit cell of at least 14 Å dimensions was used in order to prevent the interaction between clusters of different unit cells. In these calculations the Γ point was the only k point considered. The geometry of the clusters is obtained from the comparison of the experimental and DFT vibrational spectra performed in Sec. III. More precisely, the ground state geometries (3,1)A $M = 3$, (4,1)A $M = 3$, (5,1)C $M = 0$, (6,1)B $M = 1$, (7,1)B $M = 0$, and (9,1)B $M = 2$ are taken. Note that for Nb_9Co the structure with C_{4v} symmetry is chosen. Namely for a magnetic cluster the Jahn-Teller distortion should be counteracted by the exchange interaction between Nb and Co.

The effective on-site Coulomb repulsion U between the $3d$ electrons of the Co impurity is obtained from DFT calculations in conjunction with the random phase approximation (RPA) within the full-potential linearized augmented plane wave (FLAPW) method [55]. All these calculations are performed with the GGA functional as formulated by Perdew, Burke, and Ernzerhof [40]. Here a large unit cell of at least 12 Å dimensions is used and also only the Γ point is considered. Further, the plane wave cutoff is 4.0 bohr^{-1}. The actual RPA calculations are performed with the SPEX code, which uses the DFT calculations as an input [56]. The SPEX code uses the Wannier90 library to construct the maximally localized Wannier functions [57,58]. For this construction five $3d$ states and one $4s$ state are used for the Co atom.

TABLE II. The Co impurity energy level E_d, broadening of the impurity level 2Γ, energy gap E_g (HOMO-LUMO gap) of the bare Nb_x host, and the effective on-site Coulomb interaction U between the Co impurity $3d$ electrons within RPA for different Nb_xCo clusters. The sixth column contains a rough estimate of the Kondo temperature T_K obtained from Eq. (5). For convenience also the experimentally observed total magnetic moment in μ_B is presented in the last column.

Cluster	E_d (eV)	Γ (eV)	E_g (eV)	U (eV)	T_K (K)	M (μ_B)
Nb_3Co	−0.88	0.34	0.03	5.5	151	4.1
Nb_4Co	−0.97	0.35	1.04	5.0	133	5.6
Nb_5Co	−1.28	0.35	0.11	4.6	68	0.0
Nb_6Co	−1.16	0.34	0.002	4.3	81	5.3
Nb_7Co	−0.99	0.26	0.36	4.1	37	0.0
Nb_9Co	−1.42	0.33	0.02	3.8	55	2.4

C. Results: Anderson impurity model

Table II presents for each Nb_xCo cluster its characteristic parameters related to the Anderson impurity model. The center of gravity of the Co $3d$ projected density of states E_d and its weighted standard deviation Γ are shown. Also are shown the band gap (HOMO-LUMO gap) E_g of the bare Nb_x host for the geometry it has in the full Nb_xCo cluster and the effective on-site Coulomb interaction U between the Co $3d$ electrons. Although Eq. (5) is strictly speaking only valid for an impurity in a nonmagnetic metallic host at half filling in the limit of small hybridization, we employed it to obtain a rough estimate of the Kondo temperature T_K for the Nb_xCo clusters. For convenience also the experimentally observed magnetic moment [see Fig. 1(d)] is presented in the last column. As can be observed, the impurity energy level E_d and its broadening 2Γ are more or less constant as a function of cluster size. On the other hand, the band gap of the bare Nb_x host strongly fluctuates as a function of cluster size, while the effective on-site Coulomb repulsion slowly decreases as a function of cluster size.

As naively expected from Refs. [14,15], the magnitude of the local Co moment should follow the trend of the band gap of the isolated host as a function of cluster size. In other words a small band gap is expected for the clusters with zero magnetic moment, while a larger band gap is expected for the magnetic clusters. It is clear that this expectation is not verified by the results in Table II. For example, magnetic Nb_3Co and Nb_6Co have a very small band gap compared with the nonmagnetic Nb_5Co and Nb_7Co clusters.

It is also interesting to have an inspection of the criterion for the existence of a local moment in the Anderson impurity model. In the case of an impurity with degenerate orbitals the criterion stated above is slightly modified into $(U + 4J)/\Gamma > \pi$, where J is the Hund exchange coupling between the impurity electrons. Even when the contribution of J is neglected, it is clear from Table II that the criterion is satisfied for all clusters. It was already known from Ref. [15] that a magnetic impurity moment can occur even when the criterion above is not satisfied. However, it appears that the other way around is also possible; i.e., there is no magnetic moment even when the criterion is satisfied.

Only considering the band gap of the bare host did not provide an explanation for some Nb_xCo clusters being magnetic and others nonmagnetic. On the other hand for Au_xCr$^+$ it perfectly predicted the magnetic moment as function of cluster size. The reason is that the Au_x host is inert; i.e., there is only a small coupling between the Cr impurity states and Au_x host states. Therefore, Au_x clusters can be considered to be in the regime $V \ll E_g$, where the size of the local moment solely depends on the band gap of the host and not on the exact positions of its energy levels. This is also apparent from the observation that for the Au_xCr$^+$ clusters the local moment of the Cr impurity is barely reduced by the interactions with the Au_x host. Contrary to the Nb_xCo clusters the magnetic moment strongly fluctuates as function of cluster size, which hints at the direction that we are in, in the regime $V \sim E_g$. Unfortunately, this cannot be directly verified from the parameters presented in Table II. Namely, Γ corresponds to the effective hybridization in which both V and the density of states of the host are involved. However, indirectly one could argue that the Nb_xCo clusters are in the $V \sim E_g$ regime. From Ref. [14] it is known that for $V \gg E_g$ the impurity moment is almost completely absent, while for $V \ll E_g$ the moment should follow the size of the band gap. Since neither of the two is in agreement with the results of Table II, it is expected that the Nb_xCo clusters are in the $V \sim E_g$ regime.

In the $V \sim E_g$ regime the exact positions of the host energy levels are known to be important. It would be helpful to be a bit more specific and to have a feeling for which host energy levels are important. For example, intuitively one would expect only host states within a range of about V around the Fermi level (chemical potential) to be important.

In order to verify this expectation we investigated the Anderson impurity model for an impurity with a single orbital coupled to 6 spin-degenerate bath states. The impurity energy level and on-site Coulomb repulsion were chosen such that the single- and double-occupied isolated impurity states are symmetric around the chemical potential, e.g., $E_d = -1$ and $U = 3$. Further, a total occupation (impurity plus bath) of 7 electrons was considered. The Anderson impurity model was solved exactly via exact diagonalization. Note that in Ref. [14] a tight-binding approximation was employed.

In Table III the influence of different arrangements of 3 occupied and 3 unoccupied (occupied and unoccupied refer to the bare bath situation) spin-degenerate host states on the impurity magnetic moment is presented. For all calculations $V = 0.1$ is taken. Columns 2 to 7 correspond to the positions of the spin-degenerate occupied and unoccupied host states, column 8 contains the band gap, and the last column the magnetic moment on the impurity. From this table it is clear that indeed only host states within a range of V are important in terms of the magnitude of the impurity magnetic moment. For example, a comparison of the first 5 calculations shows this. Also a comparison of the calculations 3, 8, 9, and 10 clearly indicates this. Another (trivial) observation can be made from calculations 4, 6, and 7. For these calculations the band gap is the same and the only difference is in the positions of the HOMO and LUMO levels with respect to the chemical potential. It appears that these exact positions are unimportant as long as the band gap is fixed. Finally, from calculations 3, 8, 9, and 10 it can also be concluded that not only the band gap

TABLE III. The impurity magnetic moment (last column) for different arrangements of the occupied (columns 2 to 4) and unoccupied (columns 5 to 7) spin-degenerate host states. The column with E_g contains the band gap (HOMO-LUMO gap).

	E_{occ1}	E_{occ2}	E_{occ3}	E_{unocc1}	E_{unocc2}	E_{unocc3}	E_g	M_{imp}
1	−0.5	−0.5	−0.5	0.5	0.5	0.5	1.0	0.98
2	−0.3	−0.3	−0.3	0.3	0.3	0.3	0.6	0.97
3	−0.1	−0.1	−0.1	0.1	0.1	0.1	0.2	0.78
4	−0.05	−0.05	−0.05	0.05	0.05	0.05	0.1	0.22
5	0	0	0	0	0	0	0	0
6	−0.1	−0.1	−0.1	0	0	0	0.1	0.21
7	0	0	0	0.1	0.1	0.1	0.1	0.23
8	−0.5	−0.1	−0.1	0.1	0.1	0.5	0.2	0.89
9	−0.3	−0.1	−0.1	0.1	0.1	0.3	0.2	0.88
10	−0.2	−0.1	−0.1	0.1	0.1	0.2	0.2	0.86

itself but also the number of states (density of states) involved is important.

Since the coupling strength V, the band gap, and host density of states are important for the impurity magnetic moment, it would be natural to study the hybridization function corresponding to the Co $3d$ electrons. Namely, the imaginary part of the hybridization function is proportional to the coupling strength V squared and the host density of states. Furthermore, in the regime $V \sim E_g$ the influence of the coupling of the impurity with the host cannot be considered as a (small) perturbation like in Au$_x$Cr$^+$. This coupling is already taken into account explicitly within the hybridization function.

For details on how the hybridization function projected on the Co $3d$ states is obtained, the reader is referred to Ref. [59]. In short the Nb$_x$Co cluster is first calculated self-consistently within DFT. Then, from the obtained Kohn-Sham eigenstates and energies, the corresponding Green's function is constructed. Next, this Green's function is projected on the $3d$ states. This projected Green's function $G_{mm'}(E)$ and the hybridization function of the Co $3d$ states $\Delta_{mm'}(E)$ are related by

$$G_{mm'}(E) = [E - \epsilon_{mm'} + \mu - \Delta_{mm'}(\omega)],$$

$$\text{with } \Delta_{mm'}(E) = \sum_k \frac{V_{km}^* V_{km'}}{E - \epsilon_k + \mu}. \quad (6)$$

Here, E is the energy, V_{km} represents the coupling strength of the impurity state m with bath (host) state k, $\epsilon_{mm'}$ is obtained from the local projection of the DFT Kohn-Sham Hamiltonian, and ϵ_k corresponds to the energies of the bath states. From the expression of the hybridization function in terms of the coupling strengths and bath energy levels, it is clear that different choices of them can lead to the same hybridization function and thus the Anderson impurity problem. Therefore, unless the V_{km} matrix elements are computed directly, it is hard to explicitly determine whether Nb$_x$Co corresponds to the $V \sim E_g$ regime. However, this determination is not necessary to understand the physical origin of the presence or absence of magnetism in the Nb$_x$Co clusters.

From the discussions above we know that the HOMO-LUMO gap, the density of states at the HOMO and LUMO levels, the coupling V between the impurity and host states,
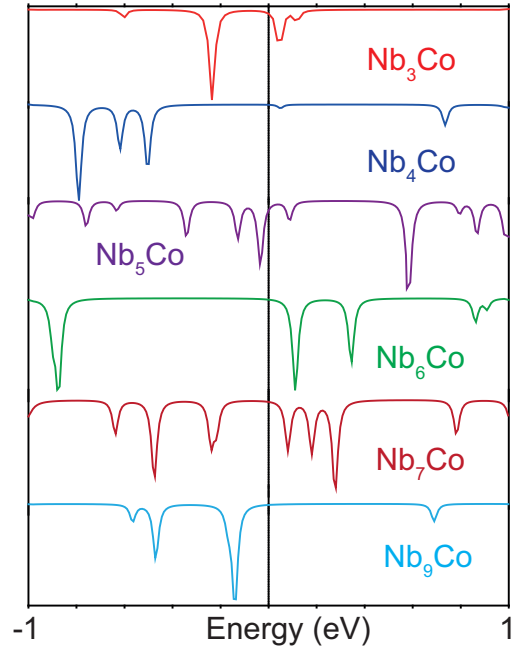

FIG. 8. The imaginary part of the hybridization function for the Co $3d$ electrons for the different Nb$_x$Co clusters.

and the on-site Coulomb repulsion U are important for the impurity magnetic moment. The first three are captured by the (imaginary part of the) hybridization function. Therefore, in Fig. 8 the imaginary part of the total [trace of $\Delta_{mm'}(E)$] hybridization function for the Co $3d$ states is shown for the different Nb$_x$Co clusters. From this figure an estimate can be made of the coupling strength V. Assuming that the peak of Nb$_3$Co at -0.25 eV is due to the coupling with only one bath state would require a V of about 0.37 eV. Therefore, the hybridization function is only plotted roughly in this range around the chemical potential (zero energy).

From the model calculations presented in Table III it is expected that a small HOMO-LUMO gap and large hybridization around the HOMO and LUMO levels is unfavorable for a magnetic moment. A discussion solely based on the hybridization functions of Fig. 8 is complicated by the fact that the on-site Coulomb repulsion is not constant over the range of clusters investigated. However, for two clusters differing only by one Nb atom in size the difference in the on-site Coulomb interaction is small. Therefore, in the following the hybridization functions will be compared cluster for cluster. From Fig. 8 it appears that Nb$_3$Co has a much stronger hybridization around the chemical potential (zero energy) than Nb$_4$Co. More precisely for Nb$_3$Co there is a peak at about -0.25 eV and 0.1 eV, while Nb$_4$Co has a peak at about -0.5 eV and a very tiny one at 0.05 eV. Since the gap between the peaks is larger and the total height of the peaks is smaller for Nb$_4$Co, a larger magnetic moment is expected for Nb$_4$Co compared to Nb$_3$Co. This is confirmed by the magnetic deflection experiment (see last column of Table II and Fig. 1).

By going from magnetic Nb$_4$Co to nonmagnetic Nb$_5$Co, it is clear that there is a huge increase of hybridization around the chemical potential. Therefore, in addition to a smaller on-site Coulomb interaction it is indeed expected that Nb$_5$Co

has a much smaller tendency to be magnetic than Nb_4Co (and Nb_3Co). Then, by going from nonmagnetic Nb_5Co to magnetic Nb_6Co, there is a huge decrease of hybridization around the chemical potential. More precisely, there is a huge increase from about 0.15 eV to 1.0 eV in the separation between the first peak below and above the chemical potential. Thus, in accordance with experiment Nb_6Co is expected to have a larger tendency to be magnetic than Nb_5Co. Next, magnetic Nb_6Co and nonmagnetic Nb_7Co will be compared. As expected the hybridization around the chemical potential is larger for Nb_7Co than for Nb_6Co. Interestingly, Nb_7Co has a hybridization around the chemical potential similar to that of Nb_3Co. However, Nb_3Co has an on-site Coulomb interaction which is 1.4 eV larger than for Nb_7Co. Finally, nonmagnetic Nb_7Co and magnetic Nb_9Co are compared. Although Nb_9Co has a quite large peak at about -0.15 eV, the difference between the first peak below and above the chemical potential is much larger. Therefore, the effective hybridization around the chemical potential is as expected smaller for Nb_9Co than for Nb_7Co. To conclude, for Nb_3Co to Nb_7Co and Nb_9Co the effective hybridization around the chemical potential is in agreement with the experimentally observed magnetic behavior.

Above we performed an analysis based on the Anderson impurity model in order to explain the experimentally observed magnetic behavior. From an inspection of the hybridization function and the on-site Coulomb repulsion a trend in agreement with experiment could be predicted. However, based on these observations it cannot be explained whether the local Co moment is absent or Kondo screened. Therefore, we made an estimate of the Kondo temperature for the clusters from Eq. (5), which are presented in the sixth column of Table II. In the case in which the nonmagnetic clusters occur due to a complete Kondo screening, higher Kondo temperatures are expected for the nonmagnetic clusters than for the magnetic clusters. From Table II it can be observed that the results are not in accordance with this expectation. For example, the highest Kondo temperatures are observed for magnetic Nb_3Co and Nb_4Co. Further, nonmagnetic Nb_5Co and Nb_7Co have a smaller Kondo temperature than magnetic Nb_6Co.

In addition we searched for signatures of the Kondo effect in the Nb_xCo clusters from the experimental side. For this purpose the temperature dependence of the magnetic deflection experiments was investigated. In the case of the Kondo effect it is expected that by approaching the Kondo temperature from below the screening of the local Co moment is reduced. An inspection of Table II shows that Nb_5Co has a Kondo temperature of 68 K and Nb_7Co of 37 K. However, even for temperatures up to 70 K both clusters still appeared to be strictly nonmagnetic, see Fig. 1(b), where Nb_5Co shows no deflection at all at 70 K. These results indeed indicate that the Kondo effect is not responsible for Nb_5Co and Nb_7Co to appear nonmagnetic.

Finally, we would like to summarize the results and put them in a broader perspective. It did not work to directly correlate (in the spirit of Ref. [15]) the size of the HOMO-LUMO gap with the observed magnetic behavior for the Nb_xCo clusters. However, the effective hybridization strength around the chemical potential does follow the observed magnetic behavior. More precisely, magnetism is favored when the effective hybridization around the chemical potential is

small, while the absence of magnetism is signaled by a large effective hybridization around the chemical potential. It should be mentioned that all these observations are in accordance with the general physical principles behind the Anderson impurity model, i.e., the Anderson criterion [$U/\Gamma > \pi$, where $2\Gamma = \pi V^2 \rho(E_F)$ is the effective hybridization]. The Anderson criterion states that a small on-site Coulomb interaction U (at the impurity site) and a large effective hybridization around the chemical potential (E_F for solids) are not favorable for a local magnetic moment to form. We would like to emphasize that this concerns general physical principles, which are not related to a specific material. To continue our discussion, it appears that for Nb_xCo clusters with $x \geqslant 14$ the effective hybridization around the chemical potential has become so strong that no local Co magnetic moment forms. The only mechanism that leads to a magnetic moment for these clusters is the presence of an unpaired electron.

V. CONCLUSION

In this work we performed magnetic deflection experiments on Co-doped Nb clusters from which we made the interesting observation that some clusters are strongly magnetic, while others are nonmagnetic. Further, it appeared that the magnetic behavior of the clusters could be divided into two regimes. For Nb_xCo clusters with $x \geqslant 14$, the magnetic to nonmagnetic behavior is exactly determined by having an odd or even number of atoms in the cluster, i.e., having an unpaired electron or not. Note that this behavior was also observed for pure Nb clusters. Then, in the region $x < 14$ strong fluctuations in the magnetic moment as function of cluster size are observed in contradiction with the odd/even behavior described above.

There are in principle two possible explanations for some clusters being nonmagnetic. Either the local moment at the Co site is absent or it is screened by the delocalized electrons of the cluster, i.e., the Kondo effect. In order to reveal the physical origin, we conducted a combined theoretical and experimental investigation.

First, we made a comparison of the experimental vibrational spectra with those obtained from a DFT study. This served two purposes. It provides the ground state geometry of the clusters. Further, due to the dependence of the vibrational spectrum on the magnetic moment, the performance of DFT in predicting the magnetic moments can be investigated. We found that not for all clusters it could be determined which calculated vibrational spectrum has the best agreement with experiment. However, for those for which it could, two interesting observations could be made. The best match with experiment not always corresponds to the geometry and magnetic state found to be the lowest in energy, ground state, in DFT. Further, we found that the DFT magnetic moments were considerably smaller than those obtained from the magnetic deflection experiments. This is due to a neglect of the orbital moments in our DFT calculations and underestimation of the spin moments within DFT.

Second, with the obtained ground state structures as an input we performed an analysis based on the Anderson impurity model. It appears that the nonmagnetic clusters are due the absence of the local Co moment and not due to the Kondo effect. In addition, the magnetic behavior of the Nb_xCo clusters can be understood from an inspection of their electronic structure.

Here magnetism is favored when the effective hybridization around the chemical potential is small, while the absence of magnetism is signaled by a large effective hybridization around the chemical potential.

Thus, DFT cannot provide a quantitative description of the magnetic moments in agreement with the deflection experiments. However, DFT can be employed to obtain a qualitative understanding of the experimentally observed magnetic moments by using its results as an input for an analyses based on the Anderson impurity model. In order to also obtain theoretically a quantitative agreement with experiment we argue that a proper consideration of correlation effects is required. For example, for DFT in combination with the dynamical mean-field theory it has recently been demonstrated to give orbital and spin magnetic moments in good agreement with experiment for pure Co clusters [29].

[1] E. Dagotto, Rev. Mod. Phys. **66**, 763 (1994).

[2] J. M. Tranquada, B. J. Sternlieb, J. D. Axe, Y. Nakamura, and S. Uchida, Nature (London) **375**, 561 (1995).

[3] K. Yamada, C. H. Lee, K. Kurahashi, J. Wada, S. Wakimoto, S. Ueki, H. Kimura, Y. Endoh, S. Hosoya, G. Shirane, R. J. Birgeneau, M. Greven, M. A. Kastner, and Y. J. Kim, Phys. Rev. B **57**, 6165 (1998).

[4] J. Fontcuberta, B. Martínez, A. Seffar, S. Piñol, J. L. García-Muñoz, and X. Obradors, Phys. Rev. Lett. **76**, 1122 (1996).

[5] A. Zylbersztejn and N. F. Mott, Phys. Rev. B **11**, 4383 (1975).

[6] M. I. Katsnelson, V. Yu. Irkhin, L. Chioncel, A. I. Lichtenstein, and R. A. de Groot, Rev. Mod. Phys. **80**, 315 (2008).

[7] R. Willett, J. P. Eisenstein, H. L. Störmer, D. C. Tsui, A. C. Gossard, and J. H. English, Phys. Rev. Lett. **59**, 1776 (1987).

[8] R. G. R. Stewart, Rev. Mod. Phys. **56**, 755 (1984).

[9] A. W. Castleman and S. N. Khanna, J. Phys. Chem. **113**, 2664 (2009).

[10] M. König, S. Wiedmann, C. Brüne, A. Roth, H. Buhmann, L. W. Molenkamp, X.-L. Qi, and S.-C. Zhang, Science. **318**, 766 (2007).

[11] X. Michalet, F. F. Pinaud, L. A. Bentolila, J. M. Tsay, S. Doose, J. J. Li, G. Sundaresan, A. M. Wu, S. S. Gambhir, and S. Weiss, Science **307**, 538 (2005).

[12] J. Friedel, Philos. Mag. **43**, 153 (1952).

[13] A. C. Hewson, *The Kondo Problem to Heavy Fermions*, edited by D. Edwards and D. Melville (Cambridge University Press, Cambridge, 1993).

[14] K. Hirsch, J. T. Lau, and B. v. Issendorff, arXiv:1407.2018v1.

[15] K. Hirsch, V. Zamudio-Bayer, A. Langenberg, M. Niemeyer, B. Langbehn, T. Möller, A. Terasaki, B. v. Issendorff, and J. T. Lau, Phys. Rev. Lett. **114**, 087202 (2015).

[16] L. Peters, E. Şaşıoğlu, S. Rossen, C. Friedrich, S. Blügel, and M. I. Katsnelson, Phys. Rev. B **95**, 155119 (2017).

[17] R. Moro, X. Xu, S. Yin, and W. A. de Heer, Science **300**, 1265 (2003).

[18] R. Moro, S. Yin, X. Xu, and W. A. de Heer, Phys. Rev. Lett. **93**, 086803 (2004).

[19] A. Diaz-Bachs, M. I. Katsnelson, and A. Kirilyuk, New J. Phys. **20**, 043042 (2018).

[20] A. Fielicke, C. Ratsch, G. von Helden, and G. Meijer, J. Chem. Phys. **127**, 234306 (2007).

[21] A. Pramann, K. Koyasu, A. Nakajima, and K. Kaya, Int. J. Mass Spectrom. **229**, 77 (2003).

[22] H. Li, X. Kuang, L. Ding, P. Shao, L. Han, and T. Lu, Int. Comput. Mater. Sci. **95**, 600 (2014).

[23] O. Stern and W. Gerlach, Ann. Phys. **74**, 673 (1924).

[24] P. Milani and W. A. de Heer, Rev. Sci. Instrum. **61**, 1835 (1990).

[25] I. I. Rabi, J. M. Kellog, and J. R. Zacharias, Phys. Rev. **46**, 157 (1934).

[26] X. Xu, S. Yin, R. Moro, and W. A. de Heer, Phys. Rev. Lett. **95**, 237209 (2005).

[27] F. W. Payne, W. Jiang, J. W. Emmert, J. Deng, and L. A. Bloomfield, Phys. Rev. B **75**, 094431 (2007).

[28] X. Xu, S. Yin, R. Moro, and W. A. de Heer, Phys. Rev. B **78**, 054430 (2008).

[29] L. Peters, I. Di Marco, O. Grånäs, E. Şaşıoğlu, A. Altun, S. Rossen, C. Friedrich, S. Blügel, M. I. Katsnelson, and A. Kirilyuk and O. Eriksson, Phys. Rev. B **93**, 224428 (2016).

[30] A. Langenberg, K. Hirsch, A. Lawicki, V. Zamudio-Bayer, M. Niemeyer, P. Chmiela, B. Langbehn, A. Terasaki, B. V. Issendorff, and J. T. Lau, Phys. Rev. B **90**, 184420 (2014).

[31] J. Minár, S. Bornemann, O. Šipr, S. Polesya, and H. Ebert, Appl. Phys. A **82**, 139 (2006).

[32] I. M. L. Billas, A. Châtelain, and W. A. de Heer, J. Magn. Magn. Mater. **168**, 64 (1997).

[33] Q. Ma, Z. Xie, J. Wang, Y. Liu, and Y. Li, Phys. Lett. A **358**, 289 (2006).

[34] J. M. Bakker, V. J. F. Lapoutre, B. Redlich, J. Oomens, B. G. Sartakov, A. Fielicke, G. von Helden, G. Meijer, and A. F. G. van der Meer, J. Chem. Phys. **132**, 074305 (2010).

[35] M. Haertelt, V. J. F. Lapoutre, J. M. Bakker, B. Redlich, D. J. Harding, A. Fielicke, and G. Meijer, J. Phys. Chem. Lett. **2**, 1720 (2011).

[36] J. Jalink, J. M. Bakker, Th. Rasing, and A. Kirilyuk, J. Phys. Chem. Lett. **6**, 750 (2015).

[37] G. Kresse and J. Furthmüller, Phys. Rev. B **54**, 11169 (1996).

[38] P. E. Blöchl, Phys. Rev. B **50**, 17953 (1994).

[39] G. Kresse and D. Joubert, Phys. Rev. B **59**, 1758 (1999).

[40] J. P. Perdew, K. Burke, and M. Ernzerhof, Phys. Rev. Lett. **77**, 3865 (1996).

[41] R. L. Johnston, Dalton Trans. **0**, 4193 (2003).

[42] R. Logemann, G. A. de Wijs, M. I. Katsnelson, and A. Kirilyuk, Phys. Rev. B **92**, 144427 (2015).

[43] P. W. Anderson, Phys. Rev. **124**, 41 (1961).

[44] A. M. Tsvelick and P. B. Wiegmann, Adv. Phys. **32**, 453 (1983).

[45] T. K. Ng and P. A. Lee, Phys. Rev. Lett. **61**, 1768 (1988).

[46] Y. Meir, N. S. Wingreen, and P. A. Lee, Phys. Rev. Lett. **70**, 2601 (1993).

[47] N. S. Wingreen and Y. Meir, Phys. Rev. B **49**, 11040 (1994).

[48] S. M. Cronenwett, T. H. Oosterkamp, and L. P. Kouwenhoven, Science **281**, 540 (1998).

[49] D. Goldhaber-Gordon, H. Shtrikman, D. Abusch-Magder, D. Mahalu, U. Meirav, and M. A. Kastner, Nature (London) **391**, 156 (1998).

[50] F. D. M. Haldane and P. W. Anderson, Phys. Rev. B **13**, 2553 (1976).

[51] P. Hohenberg and W. Kohn, Phys. Rev. **136**, B864 (1964).

[52] W. Kohn and L. J. Sham, Phys. Rev. **140**, A1133 (1965).

[53] J. M. Wills, M. Alouani, P. Andersson, A. Delin, O. Eriksson, and O. Grechnyev, *Full-Potential Electronic Structure Method* (Springer-Verlag, Berlin, 2010).

[54] J. P. Perdew and Y. Wang, Phys. Rev. B **45**, 13244 (1992).

[55] See http://www.flapw.de.

[56] C. Friedrich, S. Blügel, and A. Schindlmayr, Phys. Rev. B **81**, 125102 (2010).

[57] A. A. Mostofi, J. R. Yates, Y.-S. Lee, I. Souza, D. Vanderbilt, and N. Marzari, Comput. Phys. Commun. **178**, 685 (2008).

[58] F. Freimuth, Y. Mokrousov, D. Wortmann, S. Heinze, and S. Blügel, Phys. Rev. B **78**, 035120 (2008).

[59] O. Grånäs, I. Di Marco, P. Thunström, L. Nordström, O. Eriksson, T. Björkman, and J. M. Wills, Comput. Mater. Sci. **55**, 295 (2012).